Facile synthesis of magnetically separable $CoFe_2O_4/Ag_2O/Ag_2CO_3$ MARK nanoheterostructures with high photocatalytic performance under visible light and enhanced stability against photodegradation

Andris Šutka[a,b,], Nicola Döbelin[c], Urmas Joost[b], Krisjanis Smits[d], Vambola Kisand[b], Mihael Maiorov[e], Kuno Kooser[b,f], Mati Kook[b], Roberto Felix Duarte[g], Tanel Käämbre[b]

[a] Research Laboratory of Functional Materials Technologies, Faculty of Materials Science and Applied Chemistry, Riga Technical University, P. Valdena 3/7, 1048 Riga, Latvia
[b] Institute of Physics, University of Tartu, W. Ostwaldi Str 1, 50411 Tartu, Estonia
[c] RMS Foundation, Bischmattstrasse 12, 2544 Bettlach, Switzerland
[d] Institute of Solid State Physics, University of Latvia, Kengaraga 8, 1063 Riga, Latvia
[e] Institute of Physics, University of Latvia, Miera 32, 2169 Salaspils, Latvia
[f] Department of Physics and Astronomy, University of Turku, FIN-20014 Turku, Finland
[g] Helmholz-Zentrum Berlin für Materialien und Energie GmbH, 14109 Berlin, Germany

ARTICLE INFO

Keywords:
Silver oxide
Silver carbonate
Photocatalytic
Nanoheterostructures
Magnetic

ABSTRACT

We have developed magnetically separable and reasonably stable visible light active photocatalysts containing $CoFe_2O_4$ and mixture of Ag_2O/Ag_2CO_3 nanoheterostructures. Obtained ternary nanoheterostructures outperform previously reported magnetically separable visible light photocatalysts, showing one of the highest visible light photocatalytic dye degradation activities in water by a magnetically separable photocatalyst. Photocatalytically active part is Ag_2O/Ag_2CO_3 whereas the $CoFe_2O_4$ mainly has stabilizing and magnetic separation functions. The Ag_2CO_3 phase junction on Ag_2O nanoparticle surface were obtained by straightforward phase transformation from silver oxide to silver carbonate in air due to ambient CO_2. The phase transformation was followed using X-ray diffraction (XRD), and hard X-ray photoelectron spectroscopy (HAXPES) measurements.

1. Introduction

The widespread environmental pollution has surpassed the threshold of natural purification and has become an urgent task that needs to be accomplished [1]. Conventional purification methods such as chlorination, ozonation and UV irradiation requires the use of chemical reagents or external energy supply. Photocatalytic water purification by oxide semiconductor photocatalysts has been recognized as a green, reagent free and zero energy technology, because it does not require chemical additives, energy consumption and the same materials potentially can be used repeatedly [2]. In its simplest form semiconductor oxide nanopowders are dispersed in wastewater and the suspension is exposed to sunlight. Absorbed photons excite electrons to the conduction band and leave holes in the valence band of semiconductor oxides, thus creating photogenerated elec-tron–hole pairs, which in turn trigger reduction and oxidation reactions on the photocatalyst nanoparticle surface and the formation of reactive oxygen species into the water [3].

Silver based semiconductor photocatalysts such as silver halogens [4–6], Ag_3PO_4 [7], Ag_2CO_3 [8], Ag_2O [9], Ag_3AsO_4 [10], $AgGaO_2$ [11], Ag_2CrO_4 [12] have been recognized as particularly efficient. Un-fortunately, due to the low photocorrosion resistance of the silver compounds their photocatalytic activity deteriorates strongly over time and limits their practical applications. Recently, Yu et al. reported especially high visible light photocatalytic activity and some photo-corrosion stability for two different silver semiconductors Ag_2O and Ag_2CO_3 coupled into a heterostructure with the enhanced charge car-rier separation [13]. Ag_2CO_3 has a more positive potential of the con-duction band (CB: 0.27 V at standard hydrogen potential (SHE) and pH = 0) and valence band (VB: 2.77 V) than that of Ag_2O (CB: 0.20 V, VB: 1.5 V), thus satisfying conditions for photogenerated charge separation. Photogenerated electrons are accumulated in Ag_2CO_3 while holes in Ag_2O [13]. By electron transfer to Ag_2CO_3, the Ag_2O is pro-tected from reduction ($Ag_2O \rightarrow 2Ag + 1/2O_2$), increasing the overall stability of the heterostructure.

.

Ag_2O/Ag_2CO_3 heterostructure was obtained before [13] via phase transformation route by controlled oxidation of Ag_2CO_3 in air by heating at 220 °C. In the present investigation, Ag_2O/Ag_2CO_3 hetero-structures have been successfully synthesized by an alternative straightforward phase transformation route where Ag_2CO_3 forms at precipitated Ag_2O during post-synthesis drying at 60 °C in ambient air atmosphere due to presence of CO_2. The stability of Ag_2O/Ag_2CO_3 photocatalyst was further strongly enhanced by adding $CoFe_2O_4$. Cobalt ferrite as a ferrimagnetic compound is supplementary useful for nano-powder recycling from solution after photocatalytic reactions, as the recovery efficiency is relevant for practical recurrent use of nano-powder photocatalysts [14].

2. Experimental

2.1. Materials

Silver nitrate ($AgNO_3$, 99%), cobalt nitrate hexahydrate ($Co(NO_3)_2 \cdot 6H_2O$, > 99%), iron(III) nitrate nonahydrate ($Fe(NO_3)_3 \cdot 9H_2O$, > 98%), sodium hydroxide (NaOH, > 98%) and methy-lene blue (MB) were purchased from Sigma- Aldrich. All solutions were prepared with deionized water (Milli–Q, electrical resistivity 18.2 MΩ cm).

2.2. Ag_2O/Ag_2CO_3 nanoheterostructure synthesis

Silver nitrate 35 mM and NaOH 0.2 M water solutions were pre-pared and mixed at volume ratio 1:1 at room temperature by magnetic stirring for 30 min. Obtained precipitates were centrifuged and se-quentially washed by water for five times. Washed samples were fil-tered on Fluoropore™ PTFE filter membranes (pore size 0.2 μm, diam. 47 mm (Sigma)) and dried at 60 °C for 24 h in ambient atmosphere.

2.3. $CoFe_2O_4$ synthesis

Cobalt ferrite $CoFe_2O_4$ was synthetized by co-precipitation method as described in our previous work [15]. Briefly, cobalt nitrate 0.2 M and iron nitrate 0.4 M water solutions were mixed in volume ratio 1:1 and 5 M NaOH aqueous solution was added at room temperature dropwise under constant stirring until reaching pH > 13. The mixture was then heated up to 80 °C and stirred for 3 h in a capped glass vial. The pre-cipitates obtained were washed with Milli-Q water for five times and dried at 60 °C for 24 h.

2.4. Multicomponent $(CoFe_2O_4)_x/(Ag_2O/Ag_2CO_3)_{1-x}$ nanoheterostructure synthesis

To obtain multicomponent $(CoFe_2O_4)_x/(Ag_2O/Ag_2CO_3)_{1-x}$, nanohe-terostructure Ag_2O/Ag_2CO_3 synthesis (according to procedure de-scribed in Section 2.2) was performed in $CoFe_2O_4$ nanoparticle colloid. In order to ensure high homogeneity of heterostructures, synthesized $CoFe_2O_4$ precipitates were used directly after centrifugation based washing procedures without drying. Before silver nitrate precipitation, as-prepared $CoFe_2O_4$ nanoparticle colloid in water (100 ml) was homogenized by ultrasonification for 10 min at 100% intensity of Hielscher UP200S ultrasonic lab homogenizer. Silver nitrate water so-lution was added to $CoFe_2O_4$ colloid and precipitated by adding NaOH 0.2 M solution at room temperature by magnetic stirring for 30 min. The silver nitrate molarity was maintained at molarity 35 mM. Cobalt ferrite nanoparticle concentration was maintained in order to obtain $(CoFe_2O_4)_x/(Ag_2O/Ag_2CO_3)_{1-x}$ heterostructures where x = 0.10; 0.15; 0.30; 0.50.

2.5. Materials characterisation

The crystalline phases of synthesised materials were analysed by powder X-ray diffraction (XRD) in a glass capillary of 0.5 mm in dia-meter. A D8 Advance diffractometer (Bruker, Karlsruhe, Germany) equipped with a CuKa X-ray tube and a Kβ filter in the primary beam was used to acquire datasets in a 2θ range from 17.5 to 100° with a step size of 0.0122° and a counting time of 4 s per step. The crystalline phases were identified by comparing peak positions with the PDF-4+ database [12] and quantified with Rietveld refinement using the soft-ware Profex [16]. Crystal structure templates for all identified phases were also adopted from the PDF-4+ database: Ag (PDF# 04-001-2617), $CoFe_2O_4$ (04-016-3954), Ag_2O (PDF# 04-004-5271), Ag_2CO_3 (04-012-6615).

Microstructure of nanopowders was visualised using high resolution scanning electron microscopy (SEM) (Helios Nanolab, FEI) and trans-mission electron microscopy (TEM, Tecnai G20, FEI) operated at 200 kV. Specific surface areas S (m^2/g) for synthesized materials were calculated from nitrogen adsorption–desorption isotherms (recorded by using instrument NOVA 1200e; Quantachrome, UK) by multipoint Brunauer–Emmett–Teller (BET) method.

The hard X-ray photoelectron spectroscopy (HAXPES) measure-ments (with an overall resolution of 0.4 eV) were done on the HIKE experimental station at the KMC-1 beamline at the BESSY-II synchro-tron source (Helmholtz-Zentrum Berlin, Germany) [17]. Several com-plementary X-ray photoelectron spectroscopy (XPS) measurements were done at lower photon energies (using a Mg/Al-Kα X-ray source and a Scienta SES100 analyser) in order to check the conclusions drawn from the HAXPES results. The motivation of using this technique in this study is that HAXPES appears to be one of the very few techniques that
– in nanostructures – can make distinction between surface and bulk composition possible without destroying the samples (different from sputter etch profiling, which is suitable for smooth films, but would suffer here from a macroscopically undefined initial surface).

Light absorbance of nanopowder samples was measured by Shimadzu UV–vis spectrophotometer, UV-3700 (Shimadzu Scientific Instruments Kyoto, Japan) with barium sulphate coated integrating sphere ISR-240A. A Kubelka–Munk conversion was applied to a diffuse reflectance spectrum to compensate for differences in raw diffuse re-flectance spectra from its transmission equivalent.

Magnetic properties were estimated using a vibrating sample mag-netometer (Lake Shore Cryotronic Co., Model 7404 VSM, USA).

2.6. Photocatalytic activity measurement

Photocatalytic activities and photocorrosion stability of the ob-tained samples were evaluated through the photocatalytic degradation of the typical water pollutant, MB dye in an aqueous solution under visible light irradiation, using a 100 W light-emitting diode (LED) light source (emission band approximately 415–700 nm, i.e. 2.99 eV to 1.77 eV) with effective power density 45 ± 3 mW/cm^2. Photocatalytic reactions were performed in closed 20 ml glass vials under constant stirring and room temperature air stream for cooling. The initial con-centration of MB in the reaction vials was fixed at 10 mg/l with a photocatalyst loading of 1 mg/ml. Phtocatalytic nanoparticles were dispersed in reaction vial by Hielscher UP50H Compact Lab Homogenizer at maximum intensity for 3 min. Before tests, mixed so-lutions were kept in the dark until an absorption-desorption equili-brium was observed.

The rate of the MB dye photocatalytic degradation was monitored by sampling 1.4 ml from each mixed solution after certain irradiation time intervals, centrifuging and analysing it using a spectrophotometer. Photocatalytic activities of the samples were estimated quantitatively by calculating the rate constant (k) of MB degradation by employing the pseudo-first order reaction kinetic equation $-\ln(C/C_0) = kt$, where C_0 is the absorption peak intensity of the MB in solution and C is the MB absorption peak maximum intensity after degradation for a period of time (t). To exclude the effects of shape and size of the photocatalytic particles, the pseudo-first-order rate constants, k values, were

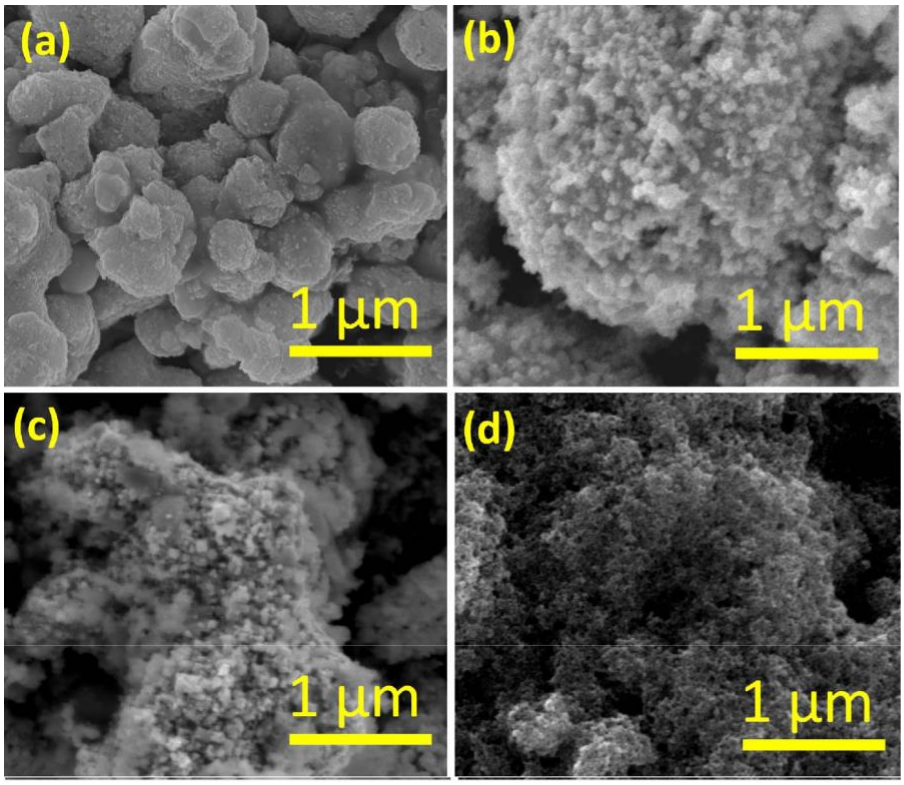

Fig. 1. SEM micrographs of various synthesized nanopowder photocatalysts: (a) Ag_2O/Ag_2CO_3; (b) and (c) multi-component $(CoFe_2O_4)_x/(Ag_2O/Ag_2CO_3)_{1-x}$ heterostructure with x = 0.10 and 0.30, respectively; (d) $CoFe_2O_4$.

3. Results and discussion

3.1. Microstructure of the synthesized nanopowders

The microstructure of the synthesized nanopowders, examined by SEM, is demonstrated in Fig. 1. All the obtained nanopowders consist of nanoparticle agglomerates where individual nanoparticle size appears to be on the order of a few tens of nanometers on average. The relatively small particle size can be explained by the overall tendency to obtain smaller sized particles at lower synthesis temperatures. The Ag2O/Ag2CO3 heterostructure was obtained by room temperature precipitation, while CoFe2O4 was co-precipitated at 80 °C. The Ag2O/Ag2CO3 nanosized dimensions were confirmed by TEM studies (Fig. 2). TEM images also demonstrate high crystallinity of synthesized Ag2O/Ag2CO3 nanoheterostructures.

3.2. Crystal structure

Fig. 3(a) demonstrates XRD diffractograms for synthesized Ag2O, Ag2O/Ag2CO3, (CoFe2O4)0.15/(Ag2O/Ag2CO3)0.85 and CoFe2O4 samples. The diffractograms demonstrated in Fig. 3(a)–(i) were measured on non-dried (washed) precipitates in water obtained by AgNO3 precipitation with NaOH:

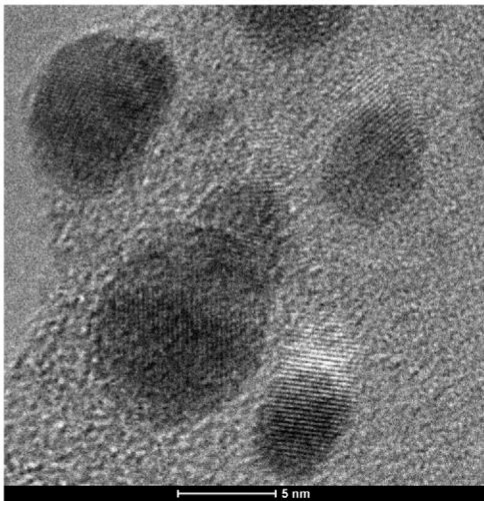

g. 2. TEM image of Ag_2O/Ag_2CO_3.

$$AgNO_3 + NaOH \rightarrow AgOH + NaNO_3 \quad (1)$$

$$AgOH + AgOH \rightarrow Ag_2O + H_2O \quad (2)$$

The diffractograms show pure Ag_2O formation in water without adjacent phases. When obtained Ag_2O is dried in ambient atmosphere at 60 °C for 24 h, adjacent peaks related to Ag_2CO_3 phase can be observed in diffractogram, plausibly due to Ag_2O reaction with atmo-spheric CO_2:

$$Ag_2O + CO_2 \rightarrow Ag_2CO_3 \quad (3)$$

It has been previously reported that upon exposure of co-pre-cipitated high surface area Ag_2O to ambient air, the content of Ag_2CO_3 in a Ag_2O sample will increase and saturate after a month at a content of 30% [18]. We have performed Rietveld analysis on a precipitated Ag_2O (stored in water) and samples stored in ambient air longer than one month. The Rietveld analysis has shown that the samples stored in water had no adjacent Ag_2CO_3 phase, while the samples stored in air contain approximately 30% Ag_2CO_3. We also obtained three component $(CoFe_2O_4)_x/(Ag_2O/Ag_2CO_3)_{1-x}$ nanoheterostructures, where the primary role of $CoFe_2O_4$ is to provide magnetic separation functions. To confirm the existence of the proposed crystalline phases the XRD data of the obtained $(CoFe_2O_4)_{0.15}/(Ag_2O/$

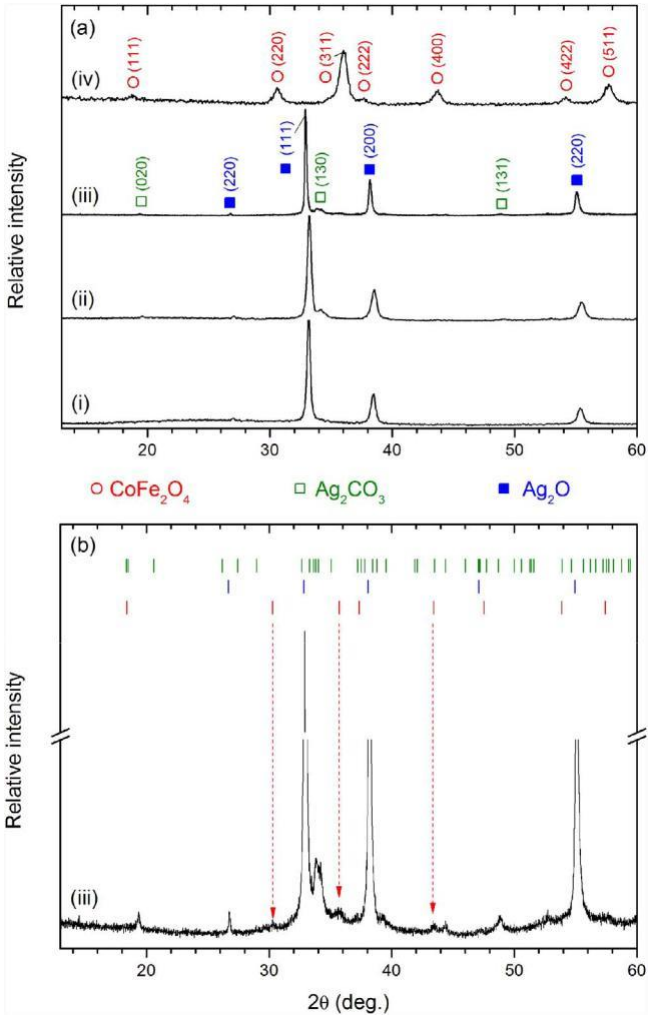

Fig. 3. XRD diffractograms of (a) silver based photocatalysts: Ag_2O (i), Ag_2O/Ag_2CO_3 (ii), $CoFe_2O_4/Ag_2O/Ag_2CO_3$ (iii) and of pristine co-precipitated $CoFe_2O_4$ (iv); (b) detailed view of the $CoFe_2O_4/Ag_2O/Ag_2CO_3$ (iii) diffractogram.

$Ag_2CO_3)_{0.85}$ nanoheterostructure is shown in Fig. 3(a)–(b). The low relative intensity of $CoFe_2O_4$ peaks can be related to small ferrite par-ticle size, but also to the high absolute intensity of the highly symmetric Ag_2O. The weak reflection peaks for room temperature co-precipitated spinel ferrites on XRD curves have been noticed recurrently, and it has been rationalized as a result of small particle size in combination with moderate crystallinity. As an example, the formation of 3 nm mean diameter $NiFe_2O_4$ particles using the same co-precipitation synthesis protocol was reported earlier [19]. Fig. 3((a)–(iv)) shows the XRD pattern of the co-precipitated $CoFe_2O_4$ powder used for the three-component heterostructure synthesis (prior to $AgNO_3$ introduction) where the pristine inverse spinel $CoFe_2O_4$ can readily be identified. Complementarily, the formation of $CoFe_2O_4$ is also confirmed by the magnetic behaviour of synthesised samples both for the pristine cobalt ferrite and the three component heterostructure (discussed further below).

3.3. Electronic structure

In order to probe the bulk composition of the heterostructured na-noparticles, hard X-ray photoelectron spectra (HAXPES) were measured from a set of samples. Fig. 4 shows HAXPES (measured at synchrotron source) and conventional XPS (measured with Mg/Al-$K\alpha$ X-ray sources) results for three different ferrite content samples, the reference samples of component materials, and of the functionally optimal x = 0.10 ferrite content sample, which was recovered from the solution after 5 photocatalytic cycles. The incident photon energies were chosen so that the resulting probe depths would allow for discrimination of surface versus bulk composition. Estimations of the photoelectron inelastic mean free path (IMFP as a measure of probe depth [20] and are given as well alongside the C 1s spectra). The data reveal sizeable carbonate content, which relatively decreases with increasing ferrite content – similar to the observed photocatalytic activity. The carbonate signal at ~288 eV [21,22] is stronger – relative to adventitious carbon signal at ~285 eV – in the less surface sensitive spectra taken at higher incident photon energy, but this reflects the fact that adventitious carbon species are present as surface adsorbants rather than a finite thickness layer. The O 1s XPS shortly below indeed shows that the carbonate layer covers the oxide component.

The Ag $3d_{5/2}$ binding energies for Ag_2CO_3 and Ag_2O (both 367.7 eV ± 0.2 eV) [20,21] and metallic silver (368.2 eV) lie rela-tively close, but the available Ag (metal) as reference sample allows to avoid most energy scale uncertainties. From the Ag 3d photoelectron spectra in Fig. 4 (middle panel) all the heterostructured samples can be traced to show oxide-like peak positions, which suggests that no sig-nificant photocorrosion has taken place.

The O 1s spectrum (Fig. 4, left panel) of the Ag_2O/Ag_2CO_3 couple shows two peaks, at approximately 529.2 eV and 530.6 eV, which align with reported O 1s binding energies in Ag_2O and Ag_2CO_3 [21–23]. The cobalt ferrite main peak is in between these two silver compounds at 529.9 eV [24,25]. The ferrite peak appears to dominate the O 1s region for the heterogeneous samples of higher ferrite content than 10%. For the latter, however the O 1s XPS shows the carbonate to dominate (both over the ferrite and the oxide), with an Ag_2O feature seen as a shoulder in the spectrum. According to the O 1s XPS taken at different incident energies (and hence, probe depths) the silver oxide appears to be deeper in the interior, covered with the carbonate (more detail and fitted spectra are given in the Supplemental Material). A crude estimate of the carbonate thickness would be approximately 3 nm (from the intensity ratios at the different probe depths).

To analyze multicomponent heterostructure in more detail, the binding energies related to Co 2p and Fe 2p are demonstrated in Fig. 5. The Fe 2p and Co 2p XPS binding energies (at approximately 711.0 eV and 798.0 eV, respectively) agree with the earlier reported values for $CoFe_2O_4$ [26]. For Fe 2p at low ferrite content, the overlapping broad Ag 3s peak dominates the spectrum. For a comparison, the top curve in Fig. 5 right panel displays the Ag 3s core level spectrum of the silver oxide/carbonate sample without any ferrite. For the 10% ferrite sample, the Fe 2p3/2 signal appears as a distinct shoulder to the Ag 3s line at the lower binding energy side.

3.4. Optical properties

Diffuse reflectance spectroscopy was utilised to study the light ab-sorbance properties and to estimate band gaps of synthesized com-pounds. Fig. 6 shows UV–vis absorption spectra (Kubelka-Munk func-tion) for the $CoFe_2O_4$, the Ag_2O/Ag_2CO_3 couple, and the ternary $(CoFe_2O_4)_{0.15}/(Ag_2O/Ag_2CO_3)_{0.85}$ heterostructure. All the materials show broad absorption bands in the visible range. Visually, all these nanopowders appear black. Generally, the experimental band gap of semiconductors can be found from $(\alpha h\nu)^{1/n}$ versus photon energy plot by extrapolating to zero a linear fit to the plot [27]. The exponent n can have values 1/2, 3/2, 2 and 3 depending on the nature of electronic transition (direct or indirect, allowed or forbidden) at the absorption edge [28]. An experimental band gap width value of 0.90 eV for pris-tine $CoFe_2O_4$ was deduced from the optical absorption $(\alpha h\nu)^{1/2}$ versus photon energy plot (Fig. 6(b)) in accordance with previous studies where $CoFe_2O_4$ has been considered an indirect band gap material [29]. The obtained band gap agrees with reported experimental values [30] and is close to the theoretical value of 0.8 eV calculated for the inverse spinel $CoFe_2O_4$ [31]. Meanwhile, both Ag_2O and Ag_2CO_3 are also

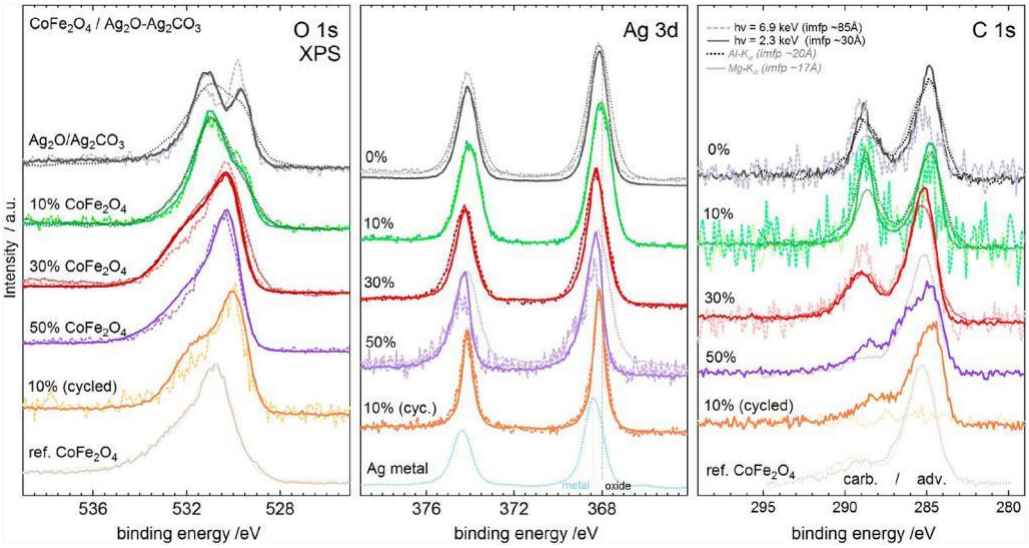

Fig. 4. HAXPES and conventional XPS spectra of O 1s, Ag 3d and C 1s measured at varied probe depth (due to varied kinetic energies) for samples with different ferrite content X.

indirect band gap semiconductors [13] and the band gap value for the Ag_2O/Ag_2CO_3 sample was found in a similar manner (Fig. 6(c)). Still, separate absorption edge features corresponding to Ag_2O and Ag_2CO_3 are seen in the $(\alpha h\nu)^{1/2}$ plot, with the 1.28 eV threshold aligning well with the generally accepted value of 1.3 eV for Ag_2O [13,32]. The higher edge at 2.24 eV in Fig. 6(c) corresponds to Ag_2CO_3 (the Ag_2CO_3 band gap has been previously reported in the 2.25–2.5 eV range) [13,33–35]. Similar absorption thresholds were observed for the ternary $(CoFe_2O_4)_{0.15}/(Ag_2O/Ag_2CO_3)_{0.85}$ heterostructure (0.80 eV, 1.26 eV and 2.40 eV corresponding to $CoFe_2O_4$, Ag_2O, and Ag_2CO_3, respectively). No absorption features related to localised surface plasmon resonance of metallic Ag were observed in the spectra.

3.5. Photocatalytic activity

Fig. 7 shows the influence of different powders on the optical den-sity change of methylene blue (MB) over visible light irradiation. The change of most intense absorption peak of MB centred at 665 nm was evaluated to study MB degradation, which was carried out as a model photocatalytic reaction under 100W light emitting diode light source emitting light in the visible range from 415 to 700 nm (i.e. 2.99 eV to 1.77 eV). No notable change of MB optical density was observed after 2 h irradiation of the MB solution in the absence of any photocatalytic sample powder. High photocatalytic activities were demonstrated by Ag_2O, Ag_2O/Ag_2CO_3 and $CoFe_2O_4/Ag_2O/Ag_2CO_3$ photocatalysts. Silver oxide Ag_2O alone destroyed all MB in solution in 1 h showing pseudo-first-order rate constant $65.21 \cdot 10^{-3}$ min^{-1}. The two component Ag_2O/Ag_2CO_3 nanoheterostructure outperformed the photocatalytic activity of Ag_2O significantly, destroying all MB in solution in less than 30 min and showing a pseudo-first-order rate constant of $180.2 \cdot 10^{-3}$ min^{-1}. In this comparison, one could consider the prob-able irreversible nanoparticle agglomeration because of capillary forces during the drying and thermal treatment steps when preparing the Ag_2O/Ag_2CO_3 sample, which would result in decreasing the specific surface area. Nevertheless, even with the potentially higher specific surface area of the pristine Ag_2O nanoparticles (as discussed above, the monophasic Ag_2O was obtained in the solution immediately after pre-cipitation, without drying the sample), the binary Ag_2O/Ag_2CO_3 na-noheterostructures show higher photocatalytic activity. We rationalise this to result from the photogenerated charge carrier separation being promoted at a Ag_2CO_3/Ag_2O heterojunction due to the suitable band alignment, as outlined above.

The three component nanoheterostructures were obtained by pre-cipitation Ag_2O into the $CoFe_2O_4$ nanoparticle colloid and drying in ambient atmosphere for Ag_2CO_3 formation on Ag_2O surface.

As concerns the ferrite component, the way it promotes the overall photocatalytic performance is not as straightforward. The co-pre-cipitated $CoFe_2O_4$ component taken alone showed no visible light photocatalytic activity. This is consistent with our previous work where photocatalytic properties of different co-precipitated spinel ferrites were studied [19] and reports by others [36–38]. A comparison of the pseudo-first-order rate constants (k values) for MB degradation and also

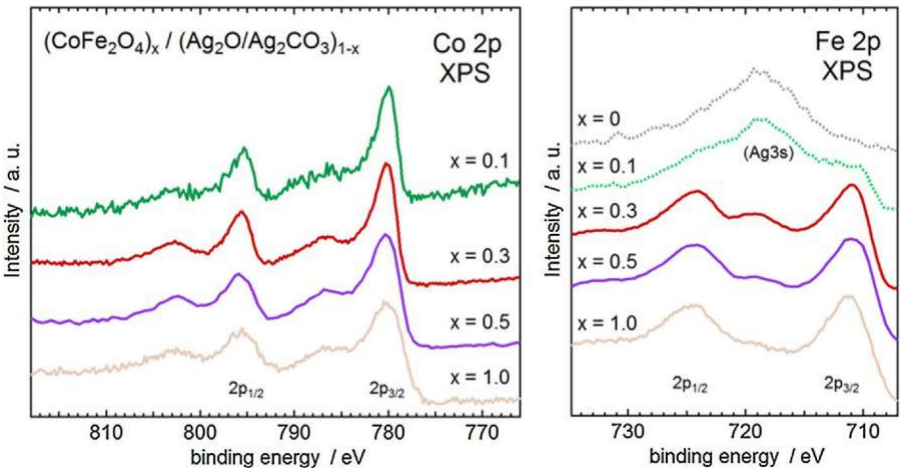

Fig. 5. The Co 2p (left panel) and Fe 2p (right panel) XPS of several samples of varied ferrite content (as labelled). The main (2p3/2) peaks are seen at 779.9 eV for Co and at 710.9 eV for Fe, which both agree with reported values for $CoFe_2O_4$.

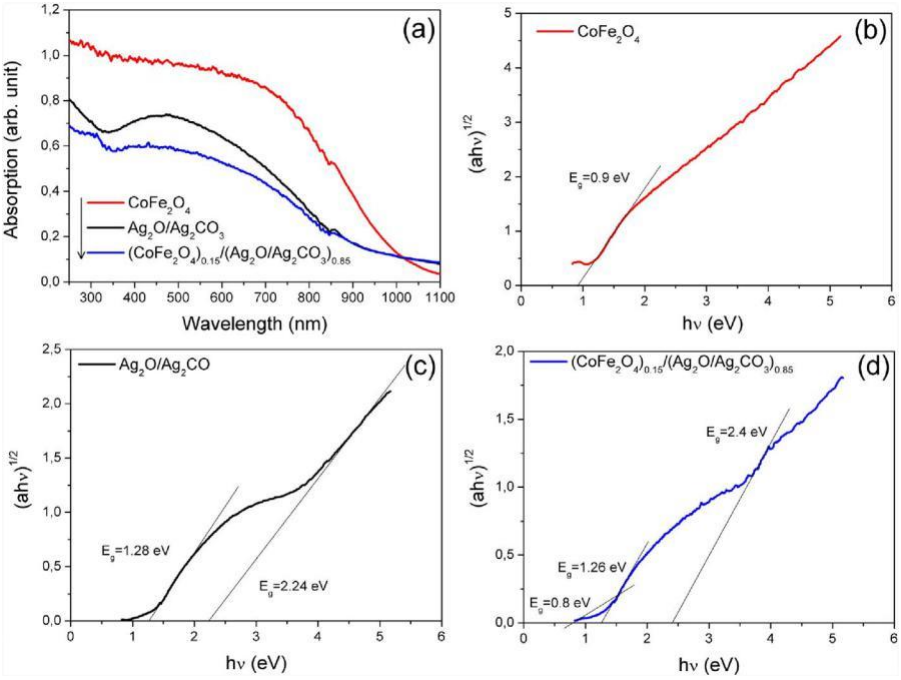

Fig. 6. The measured UV–vis absorption spectra (Kubelka–Munk function) of $CoFe_2O_4$, Ag_2O/Ag_2CO_3 and $(CoFe_2O_4)_{0.15}/(Ag_2O/Ag_2CO_3)_{0.85}$ (a) and optical absorption $(ahν)^{1/2}$ versus photon energy (hν) plots (b–d) for the same samples.

the k values normalised by the specific surface areas (Table 1), the photocatalytic activity is seen to decrease gradually when increasing the $CoFe_2O_4$ content in the three component $(CoFe_2O_4)_x/(Ag_2O/Ag_2CO_3)_{1-x}$ nanoheterostructure. Such behaviour indicates that con-sidering the photocatalytic functionality, the $CoFe_2O_4$ is not an active component. However, the MB photocatalytic degradation rate constant for the most active magnetically separable three component nanohe-terostructure was comparable to that of the pristine Ag_2O sample. For the $CoFe_2O_4/Ag_2O/Ag_2CO_3$ powder containing 10% $CoFe_2O_4$ the rate constant $30.2 \cdot 10^{-3}$ min^{-1} was observed while due to the ferrite component, the powder now was separable from the reaction medium by magnetic field. Further, our ternary nanoheterostructure outper-forms (considering relatively low intensity 100E LED light source and powder/dye concentrations) a number of previously reported magne-tically separable visible light photocatalysts, such as CdS/MFe_2O_4 (where M = Zn and Co) [39], $CoFe_2O_4$/polyaniline [40,41], $CoFe_2O_4$/ g-C_3N_4 [30,42], $CuFe_2O_4$/AgBr [43], Nd substituted $NiFe_2O_4$ [44] and we have not been able to find in the literature examples of higher visible light photocatalytic activities for magnetic field separable pho-tocatalysts.

In addition to enabling the sample to be magnetic field recovered from the solution, the inclusion of the ferrite component resulted in a significant improvement in the stability of the photocatalytic sample over several cycles. The stability estimates of the photocatalytic per-formance (Fig. 7(c)) were established by repeating the MB decoloura-tion cycles 30 min for Ag_2O/Ag_2CO_3 and 120 min for $(CoFe_2O_4)_{0.10}/$

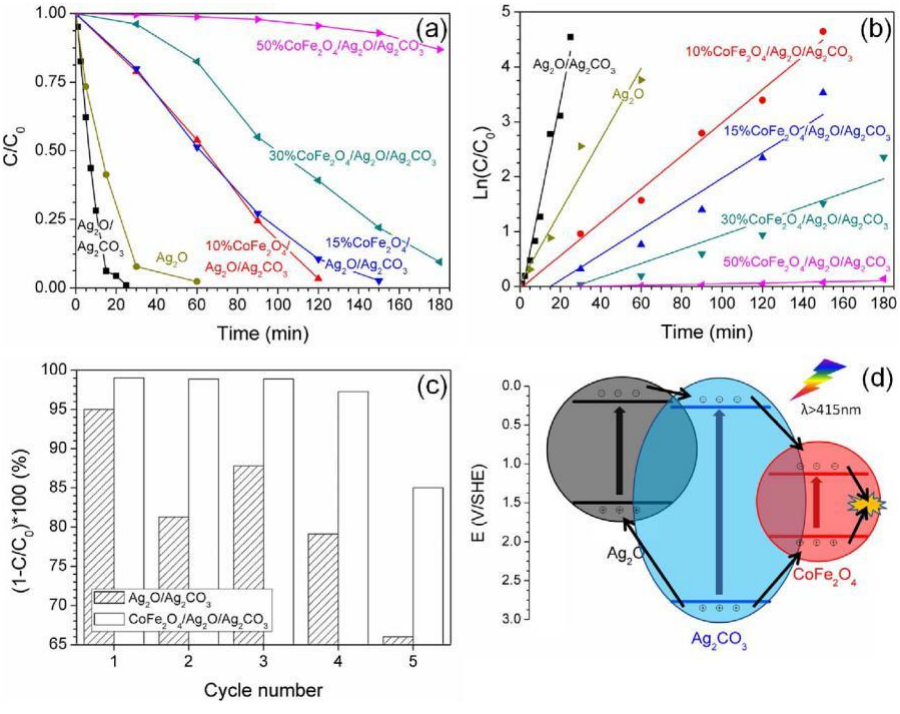

Fig. 7. Photodegradation of MB (a) and kinetic linear simu-lation curves (b) for various synthesized photocatalysts; graph (c) shows stability of Ag_2O/Ag_2CO_3 and $(CoFe_2O_4)_{0.10}/(Ag_2O/Ag_2CO_3)_{0.90}$ nanoheterostructures during photo-catalytic tests where Ag_2O/Ag_2CO_3 sample was irradiated 30 min while $(CoFe_2O_4)_{0.10}/(Ag_2O/Ag_2CO_3)_{0.90}$ sample was irradiated by 150 min per cycle; scheme (d) shows re-presentations of electron–hole separation and energy band matching of ternary $CoFe_2O_4/Ag_2O/Ag_2CO_3$ nanoheteros-tructure under visible light irradiation – potential scale (V) versus the standard hydrogen electrode (SHE) at pH = 0.

Table 1
Pseudo-first-order rate constant (k value), BET specific surface areas (S_{BET}) and k value normalised with S_{BET}.

Photocatalyst	k (min^{-1})	S_{BET} (m^2/g)	k' ($g(min^{-1}m^2)10^{-3}$)
Ag_2O	$65.21 \cdot 10^{-3}$	–	–
Ag_2O/Ag_2CO_3	$180.2 \cdot 10^{-3}$	11.89	15.16
$(CoFe_2O_4)_{0.10}/(Ag_2O/Ag_2CO_3)_{0.90}$	$30.23 \cdot 10^{-3}$	7.80	3.876
$(CoFe_2O_4)_{0.15}/(Ag_2O/Ag_2CO_3)_{0.85}$	$23.19 \cdot 10^{-3}$	15.70	1.477
$(CoFe_2O_4)_{0.30}/(Ag_2O/Ag_2CO_3)_{0.70}$	$12.81 \cdot 10^{-3}$	32.98	0.388
$(CoFe_2O_4)_{0.50}/(Ag_2O/Ag_2CO_3)_{0.50}$	$0.711 \cdot 10^{-3}$	68.26	0.010

$(Ag_2O/Ag_2CO_3)_{0.90}$. The measurements show that the introduction of the $CoFe_2O_4$ component improves stability of over the Ag_2O/Ag_2CO_3 nanoheterostructure: while the latter loses strongly in its photocatalytic performance level already during the first cycle, the $(CoFe_2O_4)_{0.10}/(Ag_2O/Ag_2CO_3)_{0.90}$ demonstrates well maintained performance at least during four consecutive cycles, even though during the photocatalytic tests the $(CoFe_2O_4)_{0.10}/(Ag_2O/Ag_2CO_3)_{0.90}$ sample was irradiated four times longer during each experimental cycle as compared to the Ag_2O/Ag_2CO_3. This can be rationalised by considering the damping of the photocorrosion effects in the silver compounds by the ferrite compo-nent. Both Ag_2O and Ag_2CO_3 have weak resistance against photo-corrosion where electrons are captured by Ag^+ ions to form metallic Ag^0 clusters [9,13]. Moreover, the photogenerated holes in Ag_2O have considerable probability to oxidise lattice O^{2-} in Ag_2O [9]. The ob-served changes in the stability with the introduction of the ferrite component suggest that the $CoFe_2O_4$ provides a recombination path for excess charge carrier on the Ag_2O/Ag_2CO_3 nanoheterostructure con-trolling the free charge carrier density and protecting silver compounds from photodecomposition. The decrease of the photocatalytic activity of ternary nanoheterostructures with the increased $CoFe_2O_4$ content appears to support such interpretation. $CoFe_2O_4$ is a narrow band gap semiconductor with both VB (+1.93) and CB (+1.13) at standard hydrogen potential (SHE) and pH = 0 [40], positioning it within the Ag_2CO_3 band gap, with also the CB potential lower than that of Ag_2O. The resulting charge transfer scheme is shown in Fig. 7(d), which shows that the band edge positions would allow most electrons from both Ag_2O and Ag_2CO_3, as well as holes from Ag_2CO_3 to proceed to $CoFe_2O_4$ [45,46]. Holes and electrons are most likely recombined in co-pre-cipitated $CoFe_2O_4$ since the compound is photocatalytically inactive.

3.6. Magnetic properties

The vibrating sample magnetometer hysteresis curves of the sam-ples are shown in Fig. 8. The Ag_2O and Ag_2O/Ag_2CO_3 exhibited para-magnetic behaviour with weak linear magnetisation in external mag-netic field. With increasing $CoFe_2O_4$ content the saturation magnetisation (M_S) gradually increases, reaching an M_S value of about 25 emu/g for the three component nanoheterostructure with $CoFe_2O_4$ content of 50%. The coercive force for the synthesized nanoheteros-tructures remained favourably low (within 100 Oe): generally, a high coercive force is considered as a drawback in photocatalytic nano-particle systems, because large remanent magnetisation can cause na-noparticle mutual attraction, triggering agglomeration and sedimenta-tion, as well as a decrease of specific surface area of the nanoparticles that can be exposed for reactions. In our case, the nanoparticle het-erostructure powders were redispersible by using an ultrasound probe. Overall, the magnetic response was strong enough for nanopowder magnetic separation from the reaction medium. Fig. 8 top left corner inset shows a photo demonstrating magnetic separation of three

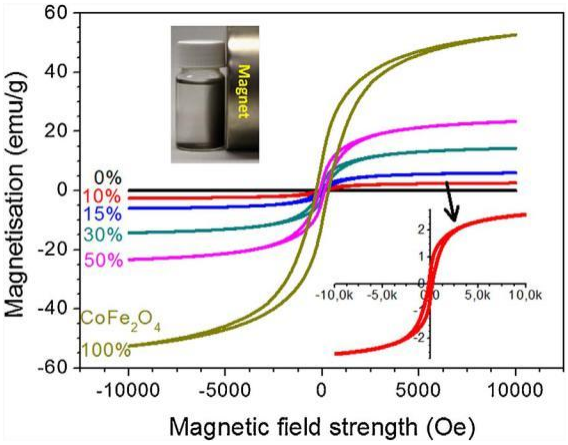

Fig. 8. Magnetisation versus magnetic field curves at room temperature for samples with different $CoFe_2O_4$ content.

component nanoheterostructure powders containing only 10% of $CoFe_2O_4$. Although the overall saturation magnetisation value of 2.5 emu/g measured for the ternary $(CoFe_2O_4)_{0.10}/(Ag_2O/Ag_2CO_3)_{0.90}$ (10% of $CoFe_2O_4$) nanoheterostructure powders seems too weak for magnetic separation, the magnetic separation occurs effectively: clear particle-free water was obtained after the separation procedure. The strong attraction to magnet is related to high saturation magnetisation 52 emu/g measured for individual $CoFe_2O_4$ nanoparticles.

4. Conclusions

Highly visible light active Ag_2O/Ag_2CO_3 nanoheterostructures can be obtained in a straightforward way by surface Ag_2O reaction with atmospheric CO_2. Ag_2O/Ag_2CO_3 nanoheterostructures exhibited an outstanding threefold increase over pristine Ag_2O in pseudo-first-order rate constant for MB degradation due to appropriate band positioning, which promotes photogenerated charge separation between the two tightly contacted silver compounds. Further ternary $(CoFe_2O_4)_x/(Ag_2O/Ag_2CO_3)_{1-x}$ nanoheterosturctures were obtained by Ag_2O precipitation in a $CoFe_2O_4$ nanoparticle suspension and subsequent partial phase transformation to Ag_2CO_3. The ternary nanoheterostructures show higher photocatalytic stability and are magnetically separable, which is relevant for practical applications. $CoFe_2O_4$ increased stability of Ag_2O/Ag_2CO_3, acting as a dynamic recombination centre for excess photo-generated charge carriers, hindering Ag_2O/Ag_2CO_3 photodegradation. Overall, the obtained ternary nanoheterostructures were at least among the most active visible light magnetically separable photocatalysts.

Acknowledgements

Riga Technical University supported the preparation of this manu-script from the Scientific Research Project Competition for Young Researchers No. ZP-2016/7. The authors wish to kindly acknowledge the financial support of HZB, Estonian Research Council (PUT1096, PUT735 and IUT2-25) and Estonian Centre of Excellence in Research Project "Advanced materials and high-technology devices for sustain-able energetics, sensorics and nanoelectronics" TK141 (2014–2020.4.01.15-0011).

.

References

[1] A.S. Adeleye, J.R. Conway, K. Garner, Y. Huang, Y. Su, A.A. Keller, Engineered nanomaterials for water treatment and remediation: costs, benefits, and applic-ability, Chem. Eng. J. 286 (2016) 640–662.

[2] S. Dong, J. Feng, M. Fan, Y. Pi, L. Hu, X. Han, M. Liu, J. Sun, J. Sun, Recent de-velopments in heterogeneous photocatalytic water treatment using visible light-responsive photocatalysts: a review, RSC Adv. 5 (2015) 14610–14630.

[3] M.A. Henderson, A surface science perspective on TiO2 photocatalysis, Surf. Sci. Rep. 66 (2011) 185–297.

[4] L. Han, P. Wang, C. Zhu, Y. Zhai, S. Dong, Facile solvothermal synthesis of cube-like Ag@AgCl: a highly efficient visible light photocatalyst, Nanoscale 3 (2011) 2931–2935.

[5] L. Kuai, B. Geng, X. Chen, Y. Zhao, Y. Luo, Facile subsequently light-induced route to highly efficient and stable sunlight-driven Ag-AgBr plasmonic photocatalyst, Langmuir 26 (2010) 18723–18727.

[6] H. Cheng, B. Huang, Y. Dai, X. Qin, X. Zhang, One-step synthesis of the nanos-tructured AgI/BiOI composites with highly enhanced visible-light photocatalytic performances, Langmuir 26 (2010) 6618–6624.

[7] Y. Bi, S. Ouyang, N. Umezawa, J. Cao, J. Ye, Facet effect of single-crystalline Ag_3PO_4 sub-microcrystals on photocatalytic properties, J. Am. Chem. Soc. 133 (2011) 6490–6492.

[8] H. Dong, G. Chen, J. Sun, C. Li, Y. Yu, D. Che, A novel high-efficiency visible-light sensitive Ag_2CO_3 photocatalyst with universal photodegradation performances: simple synthesis, reaction mechanism and first-principles study, Appl. Catal. B: Environ. 134–135 (2013) 46–54.

[9] X. Wang, S. Li, H. Yu, J. Yu, S. Liu, Ag_2O as a new visible-light photocatalyst: self-stability and high photocatalytic activity, Chem. Eur. J. 17 (2011) 7777–7780.

[10] J. Tang, Y. Liu, H. Li, Z. Tan, D. Li, A novel Ag_3AsO_4 visible-light-responsive pho-tocatalyst: facile synthesis and exceptional photocatalytic performance Chem, Commun 49 (2013) 5498–5500.

[11] Y. Maruyama, H. Irie, K. Hashimoto, Visible light sensitive photocatalyst, dela-fossite structured α-$AgGaO_2$, J. Phys. Chem. B 110 (2006) 23274–23278.

[12] S. Ouyang, Z. Li, Z. Ouyang, T. Yu, J. Ye, Z. Zou, Correlation of crystal structures, electronic structures, and photocatalytic properties in a series of Ag-based oxides: $agAlO_2$, $AgCrO_2$, and Ag_2CrO_4, J. Phys. Chem. C 112 (2008) 3134–3141.

[13] C. Yu, G. Li, S. Kumar, K. Yang, R. Jin, Phase transformation synthesis of novel Ag_2O/Ag_2CO_3 heterostructures with high visible light efficiency in photocatalytic degradation of pollutants, Adv. Mater. 26 (2014) 892–898.

[14] J. Gómez-Pastora, S. Dominguez, E. Bringas, M.J. Rivero, I. Ortiz, D.D. Dionysiou, Review and perspectives on the use of magnetic nanophotocatalysts (MNPCs) in water treatment, Chem. Eng. J. 310 (2017) 407–427.

[15] International Centre for Diffraction Data (2015). "PDF-4 +". 12 Campus Boulevard, Newtown Square, PA 19073-3273 USA.

[16] N. Doebelin, R. Kleeberg, Profex: a graphical user interface for the Rietveld re-finement program BGMN, J. Appl. Crystallogr. 48 (2015) 1573–1580.

[17] F. Schaefers, M. Mertin, M. Gorgoi, KMC-1: a high resolution and high flux soft x-ray beamline at BESSY, Rev. Sci. Instrum. 78 (2007) 123102.

[18] J.A. Allen, P.H. Scaife, Infrared spectra in the Ag2O-CO2-Ag2CO3 system, Aust. J. Chem. 19 (1966) 715–724.

[19] A. Sutka, Martins Millers, M. Vanags, U. Joost, M. Maiorov, V. Kisand, R. Pärna, I. Juhnevica, Comparison of photocatalytic activity for different co-precipitated spinel ferrites, Res. Chem. Intermed. 41 (2015) 9439–9449.

[20] S. Tanuma, C.J. Powell, D.R. Penn, Calculations of electron inelastic mean free paths. V. Data for 14 organic compounds over the 50–2000 eV range, Surf. Interf. Anal. 21 (1994) 165–176.

[21] NIST X-ray Photoelectron Spectroscopy Database, https://srdata.nist.gov/xps.

[22] J.S. Hammond, S.W. Gaarenstroom, N. Winograd, X-ray photoelectron spectro-scopic studies of cadmium- and silver-oxygen surfaces, Anal. Chem. 47 (1975) 2193–2199.

[23] V.K. Kaushik, XPS core level spectra and Auger parameters for some silver com-pounds, J. Electron Spectrosc. Relat. Phenom. 56 (1991) 273–277.

[24] N.S. McIntyre, M.G. Cook, X-ray photoelectron studies on some oxides and hydro-xides of cobalt nickel, and copper, Anal. Chem. 47 (1975) 2208–2213.

[25] G.C. Allen, K.R. Hallam, Characterisation of the spinels $M_xCo_{1-x}Fe_2O_4$ (M = Mn, Fe or Ni) using X-ray photoelectron spectroscopy, Appl. Surf. Sci. 93 (1996) 25–30.

[26] N.S. McIntyre, D.G. Zetaruk, X-ray photoelectron spectroscopic studies of iron oxides, Anal. Chem. 49 (1977) 1521–1529.

[27] A.B. Murphy, Band-gap determination from diffuse reflectance measurements of semiconductor films, and application to photoelectrochemical water-splitting, Sol. Energ. Mat. Sol. C. 91 (2007) 1326–1337.

[28] R. López, R. Gómez, Band-gap energy estimation from diffuse reflectance mea-surements on sol–gel and commercial TiO_2: a comparative study, J. Sol-Gel Sci. Technol. 61 (2012) 1–7.

[29] B.S. Holinsworth, D. Mazumdar, H. Sims, Q.-C. Sun, M.K. Yurtisigi, S.K. Sarker, A. Gupta, W.H. Butler, J.L. Musfeldt, Chemical tuning of the optical band gap in spinel ferrites: $coFe_2O_4$ vs $NiFe_2O_4$, Appl. Phys. Lett. 103 (2013) 082406.

[30] S. Huang, Y. Xu, M. Xie, H. Xu, M. He, J. Xia, L. Huang, H. Li, Synthesis of magnetic $CoFe_2O_4$/g-C_3N_4 composite and its enhancement of photocatalytic ability under visible-light, Colloids Surf. A 478 (2015) 71–80.

[31] P. Xiong, L. Wang, X. Sun, B. Xu, X. Wang, Ternary titania cobalt ferrite-polyaniline nanocomposite: a magnetically recyclable hybrid for adsorption and photo-degradation of dyes under visible light, Ind. Eng. Chem. Res. 52 (2013) 10105–10113.

[32] W. Zhou, H. Liu, J. Wang, D. Liu, G. Du, J. Cui, Ag2O/TiO2 Nanobelts hetero-structure with enhanced ultraviolet and visible photocatalytic activity, ACS Appl. Mater. Interfaces 2 (2010) 2385–2392.

[33] L. Yin, Z. Wang, L. Lu, X. Wana, H. Shi, Universal degradation performance of a high-efficiency AgBr/Ag_2CO_3 photocatalyst under visible light and an insight into the reaction mechanism, New J. Chem. 39 (2015) 4891–4900.

[34] H. Donga, G. Chen, J. Sun, C. Li, Y. Yu, D. Chen, A novel high-efficiency visible-light sensitive Ag_2CO_3 photocatalyst with universal photodegradation performances: simple synthesis, reaction mechanism and first-principles study, Appl. Catal. B: Environ. 134–135 (2013) 46–54.

[35] G. Panthi, S.-J. Park, T.-W. Kim, H.-J. Chung, S.-T. Hong, M. Park, H.-Y. Kim, Electrospun composite nanofibers of polyacrylonitrile and Ag_2CO_3 nanoparticles for visible light photocatalysis and antibacterial applications, J. Mater. Sci. 50 (2015) 4477–4485.

[36] W. Fu, H. Yang, M. Li, M. Li, N. Yang, G. Zou, Anatase TiO2 nanolayer coating on cobalt ferrite nanoparticles for magnetic photocatalyst, Matt. Lett. 59 (2005) 3530–3534.

[37] K.N. Kim, H.R. Jung, W.J. Lee, Hollow cobalt ferrite–polyaniline nanofibers as magnetically separable visible-light photocatalyst for photodegradation of methyl orange, J. Photochem. Photobiol. A: Chem. 321 (2016) 257–265.

[38] K.K. Senapati, C. Borgohain, P. Phukan, CoFe2O4–ZnS nanocomposite: a magneti-cally recyclable photocatalyst, Catal. Sci. Technol. 2 (2012) 2361–2366.

[39] P. Xiong, J. Zhu, X. Wang, Cadmium sulfide-ferrite nanocomposite as a magneti-cally recyclable photocatalyst with enhanced visible-light-driven photocatalytic activity and photostability, Ind. Eng. Chem. Res. 52 (2013) 17126–17133.

[40] P. Xiong, Q. Chen, M. He, X. Sun, X. Wang, Cobalt ferrite–polyaniline hetero-architecture: a magnetically recyclable photocatalyst with highly enhanced per-formances, J. Mater. Chem. 22 (2012) 17485–17493.

[41] K.N. Kim, H.-R. Jung, W.-J. Lee, Hollow cobalt ferrite–polyaniline nanofibers as magnetically separable visible-light photocatalyst for photodegradation of methyl orange, J. Photochem. Photobiol. A: Chem. 321 (2016) 257–265.

[42] S. Kumar, T. Surendar, B. Kumar, A. Baruah, V. Shanker, Synthesis of magnetically separable and recyclable g-C3N4-Fe3O4 hybrid nanocomposites with enhanced photocatalytic performance under visible-light irradiation, J. Phys. Chem. C 117 (2013) 26135–26143.

[43] Y. Zhao, C. Lin, H. Bi, Y. Liu, Q. Yan, Magnetically separable CuFe2O4/AgBr composite photocatalysts: preparation, characterization, photocatalytic activity and photocatalytic mechanism under visible light, Appl. Surf. Sci. 392 (2017) 701–707.

[44] K.N. Harish, H.S. Bhojya Naik, P.N. Prashanth Kumar, R. Viswanath, Optical and photocatalytic properties of solar light active Nd- substituted Ni ferrite catalysts: for environmental protection, ACS Sustain. Chem. Eng. 1 (2013) 1143–1153.

[45] H. Wang, L. Zhang, Z. Chen, J. Hu, S. Li, Z.i Wang, J. Liu, X. Wang, Semiconductor heterojunction photocatalysts: design, construction, and photocatalytic perfor-mances, Chem. Soc. Rev. 43 (2014) 5234–5244.

[46] H. Li, Y. Zhou, W. Tu, J. Ye, Z. Zou, State-of-the-art progress in diverse hetero-structured photocatalysts toward promoting photocatalytic performance, Adv. Funct. Mater. 25 (2015) 998–1013.

Institute of Solid State Physics, University of Latvia as the Center of Excellence has received funding from the European Union's Horizon 2020 Framework Programme H2020-WIDESPREAD-01-2016-2017-TeamingPhase2 under grant agreement No. 739508, project CAMART²